PROCEEDINGS OF SPIE

SPIEDigitalLibrary.org/conference-proceedings-of-spie

Investigation of ultrafast laser stress generation in fused silica, Corning Eagle XG glass, Corning ULE glass, and sapphire

Kevin Laverty, Daewook Kim, James Johnson, Michael Echter, Brandon Chalifoux

Kevin A. Laverty, Daewook Kim, James B. Johnson, Michael A. Echter, Brandon D. Chalifoux, "Investigation of ultrafast laser stress generation in fused silica, Corning Eagle XG glass, Corning ULE glass, and sapphire," Proc. SPIE 12669, Optomechanical Engineering 2023, 1266907 (28 September 2023); doi: 10.1117/12.2677619

SPIE.

Event: SPIE Optical Engineering + Applications, 2023, San Diego, California, United States

Downloaded From: https://www.spiedigitallibrary.org/conference-proceedings-of-spie on 24 Jan 2024 Terms of Use: https://www.spiedigitallibrary.org/terms-of-use

Investigation of ultrafast laser stress generation in fused silica, Corning Eagle XG glass, Corning ULE glass, and sapphire

Kevin A. Laverty[a*], Daewook Kim[a], James B. Johnson[b], Michael A. Echter[b], and Brandon D. Chalifoux[a]

[a]Wyant College of Optical Sciences, University of Arizona, 1630 E. University Boulevard, Tucson, AZ 85721
[b]Lincoln Laboratory, Massachusetts Institute of Technology, 244 Wood Street, Lexington, MA 02421

ABSTRACT

Previous work has demonstrated the feasibility of using ultrafast laser generated stress to deform fused silica substrates to a desired flatness in a process called ultrafast laser stress figuring (ULSF). Materials other than fused silica may offer superior optomechanical properties that are more suited to certain applications or environments. In this work we explore the stress generated by focused ultrafast laser pulses in several common optical materials: Corning Ultra Low Expansion (ULE) glass, Corning Eagle XG glass, fused silica, and sapphire. Using a laser polarization state perpendicular to the writing direction, we find that the laser induced stress depends on the energy of the ultrafast laser pulses, the distance between two adjacent focused pulses, and the repetition rate at which the pulses are delivered into the material. Each material explored showcases unique dependence on these parameters. The results from this investigation will be used to characterize the potential equivalent material removal rates that would be theoretically achievable by ultrafast laser stress figuring for commercially available sapphire and Eagle XG substrates.

Keywords: Stress figuring, ultrafast laser material processing, optical figuring

1. INTRODUCTION

The availability of commercial ultrafast pulsed lasers has opened avenues for many novel physical processing capabilities. By exploiting nonlinear absorption mechanisms, high intensity, short duration (femtosecond to picosecond) laser pulses allow for localized depositions of energy to occur at or near the focal region within the bulk of a dielectric material. Depending on the laser parameters (wavelength, polarization state, pulse duration, pulse energy), this localized energy deposition can lead to localized densification [1,2] or expansion [3], refractive index change [4–6], the formation of sub-wavelength periodic structures called nanogratings [7–10], or even the evolution of melt regions and voids within the material [11–14]. These resulting physical changes can be leveraged to produce unique optical devices and enable unusual manufacturing techniques.

After exposure to focused ultrafast laser pulses, many materials exhibit preferential chemical etching within the modified regions, which has been used to produce monolithic microfluidic devices in fused silica [15] and has also been used to produce embedded channels within sapphire [16]. Polarization converters [17] and high-density optical data storage devices [18] have also been produced by using the form birefringence of the resulting ultrafast laser induced nanograting structures. The ability to produce localized melt regions defined by the focal volume has additionally allowed for unique material to material welds to be achieved. Several groups have showcased the ability to weld similar glasses together [19], dissimilar dielectrics together [20], and even glasses to metals [21]. Importantly, for our group, we note that these material changes present in the focal volume of the ultrafast pulse often lead to microscale strains being generated within the bulk of the substrate [22,23]. These microscale strains and their resulting stresses produce bending moments throughout the substrate which can ultimately lead to controllable substrate curvature changes.

Previously, our group has shown that by dispersing focused ultrafast laser pulses throughout a fused silica substrate we have been able to introduce a desired corrective stress field that can appropriately flatten low- and mid-order surface height errors that were present on the wafer from fabrication and optical-coating. This process, termed ultrafast laser stress figuring (ULSF), was shown to be able to flatten a fused silica wafer (1 mm thick, 100 mm diameter) from 4.66 μm RMS down to 11 nm RMS across the first 28 Zernike terms [24]. As with conventional figuring techniques, ULSF's equivalent

*kevinlaverty@arizona.edu

Optomechanical Engineering 2023, edited by Keith B. Doyle, Brandon D. Chalifoux,
Kenneth R. Castle, José M. Sasián, Proc. of SPIE Vol. 12669, 1266907
© 2023 SPIE · 0277-786X · doi: 10.1117/12.2677619

Downloaded From: https://www.spiedigitallibrary.org/conference-proceedings-of-spie on 24 Jan 2024
Terms of Use: https://www.spiedigitallibrary.org/terms-of-use

material removal rate (eMRR) is dependent on many process parameters and exhibits material-dependent responses. In this study, we have identified several common optical materials (fused silica, Eagle XG, ULE, and sapphire) and have explored the stress-generating landscape associated with several ULSF process parameters (pulse energy, repetition rate, and pulse-to-pulse spacing). Using the information gained from this investigation, we also present eMRRs expected using ULSF for commercially available sapphire and Eagle XG wafers.

2. EQUIPMENT, MATERIALS, AND METHODOLOGY

2.1 Equipment and Materials

We used a commercial ultrafast laser (Trumpf TruMicro 2030) to generate 350 fs pulses at a central wavelength of 1030 nm with pulse energies ranging from $E_p = 150$ nJ to 3000 nJ, and repetition rates ranging from $f_{rep} =$ 225 kHz to 900 kHz. After exiting the laser, the pulse energy was fine-tuned using a half-wave plate paired with a Glan-Taylor polarizer (100,000:1 extinction ratio) and then the beam was expanded (Jenoptik BD0161) to a diameter of 8.8 mm (measured at the $1/e^2$ points). The polarization state of the laser was then controlled by using a half-wave plate, and then finally focused into the substrates using a 0.4 NA objective (Thorlabs-LMH-20X-1064). The polarization state was kept perpendicular to the writing direction for all experiments. The objective was mounted onto a z-translation stage (Aerotech PRO165SLE), allowing for fine control over the depth at which the laser pulses were focused into the samples. The samples were spring mounted onto an $x - y$ translation stage (Aerotech PlanarDL-200XY), allowing for precise application of laser pulses into the samples. A camera and a 980 nm laser diode were used to perform confocal imaging of the sample, allowing for determination of the front and back surfaces of the sample. Figure 1 shows a depiction of this laser system.

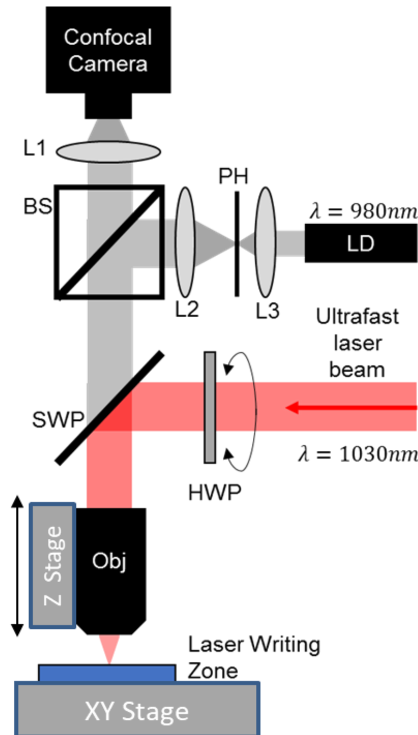

Figure 1. Laser system diagram. The expanded 1030 nm ultrafast beam is directed through a halfwave plate (HWP) to control the beam polarization state. A shortwave pass (SWP) filter directs the ultrafast pulse into the objective, which then focuses the beam into the sample. A 980 nm illumination laser diode (LD) is cleaned and expanded by lenses L3 and L2 and a pinhole (PH). A beam splitter (BS) directs the 980 nm beam through the SWP. The illumination passes through the objective and is imaged confocally onto a camera.

We used a Fizeau interferometer (Äpre Instruments S100 HR) to measure the surface height of the samples before and after modification. The samples were mounted onto steel pins with Teflon rollers which allowed for repeatable placement in front of the interferometer. Measurements were taken using the spectrally controlled interferometry external source add-

Downloaded From: https://www.spiedigitallibrary.org/conference-proceedings-of-spie on 24 Jan 2024
Terms of Use: https://www.spiedigitallibrary.org/terms-of-use

on (SpectrÄ 633 Gen 3.1), which uses a controllable low-coherence light source to selectively measure the front surface of the uncoated samples. Previous work has found that some optical coatings exhibit stresses that relax over time, leading to inconsistent measurements of surface height changes [24]. These unwanted changes in turn lead to ambiguities as to whether the modifications or the coating are responsible for the change in surface figure, so uncoated samples were used throughout this experiment.

Commercial wafers made of fused silica (JSG2, double-side polished [DSP], 100 mm diameter, 1 mm thick), Corning Eagle XG (100 mm diameter, 0.4 mm thick), Corning ULE (Standard grade, DSP, 25.4 mm diameter, 1.0 mm thick), and sapphire (c-plane, DSP, 100 mm diameter, 0.6 mm thick) were acquired. Using a Bessel beam objective (Holo/Or DeepCleave ZT Module-007-J00), 25.4 mm diameter circles with 10.5 mm flats were patterned onto the fused silica, Corning Eagle XG, and sapphire wafers using the ultrafast laser. The exposed wafers were then bathed in an 80°C potassium hydroxide bath (3M), selectively etching away the laser exposed areas. The resulting 25.4 mm samples were used for the initial parameter investigations. Prior to measurement and laser exposure, all samples were rinsed with deionized water, and wiped clean with methanol.

2.2 Laser Writing Patterns

In order to analyze the stress-generating landscape of the selected materials, we exposed the samples to a constant laser exposure pattern consisting of horizontal lines of laser modifications written across each sample at a depth of 100 µm below the surface. The horizontal lines were spaced 500 µm apart from each other in the lateral direction as depicted in Figure 2. Each horizontal line is broken into a series of individual 50 µm line segments, consisting of a 45 µm segment of laser modifications and a 5 µm segment of unmodified material. Using constant translation velocities at or below 45 mm/s, we were able to use the position synchronized output (PSO) of the stage controller and laser to produce a series of laser pulses that have very well-defined spot-to-spot spacings and repetition rates. Depending on the specified spot-to-spot spacing, the 45 µm laser modified segment could contain 900, 450, or 225 individual laser spots for 50 nm, 100 nm, or 200 nm spot-to-spot spacings respectively. For each set of parameters investigated, the write speed is dictated entirely by the product of the spot-to-spot spacing and the repetition rate.

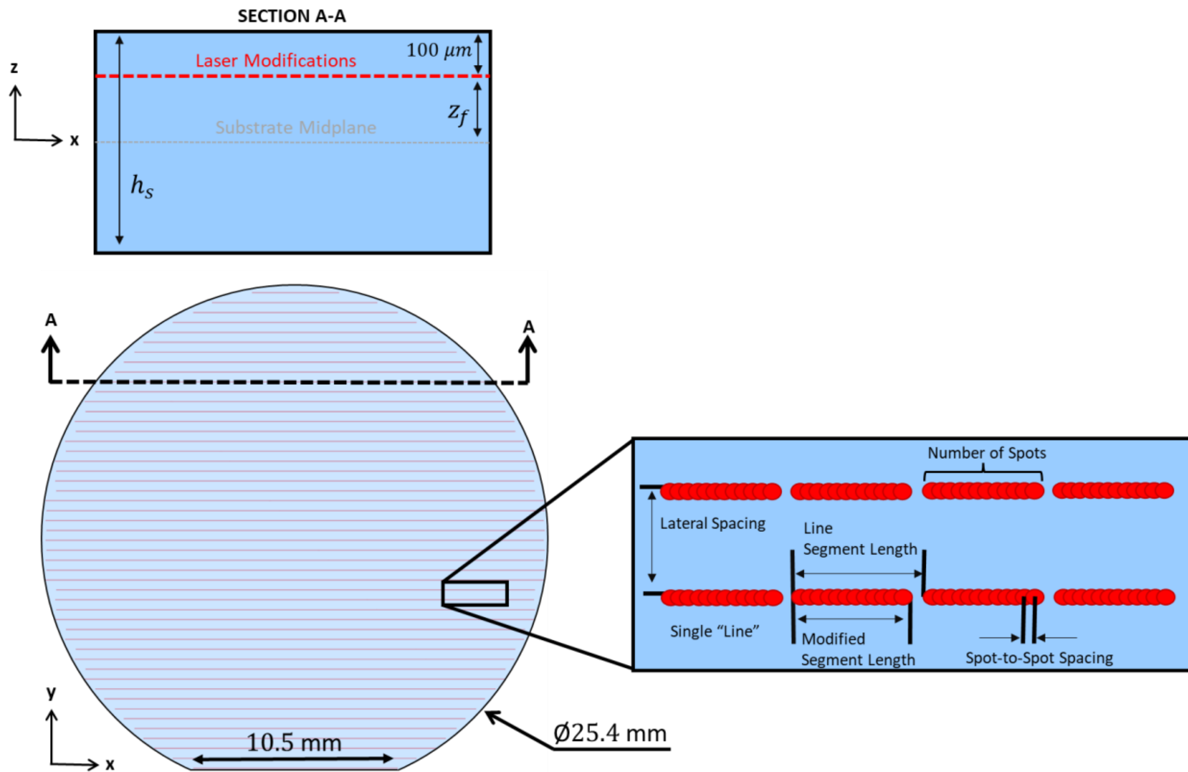

Figure 2. Depiction of wafer geometry, laser write pattern, and laser processing parameters.

Downloaded From: https://www.spiedigitallibrary.org/conference-proceedings-of-spie on 24 Jan 2024
Terms of Use: https://www.spiedigitallibrary.org/terms-of-use

2.3 Integrated Stress Determination

Similar to a stressed thin film, these modification patterns will introduce curvature changes to the substrate which can then be related back to the integrated stress associated with the modifications. Treating the set of modifications as a vanishingly thin anisotropic stressed film 100 μm below the surface of the wafer, it is possible to extract equivalent plane stress values from the measured deformation of the wafer. It is assumed that all of our substrate materials are in-plane isotropic, which allows us to use single values for the Young's modulus and Poisson's ratio for each material as shown in Table 1.

Table 1. Material properties and geometry of the samples under investigation.

Material	D (mm)	h_s(mm)	E(GPa)	ν
Sapphire	25.4	0.6	435	0.30
Corning Eagle XG	25.4	0.4	73.6	0.23
Corning ULE	25.4	1.0	67.6	0.17
Fused Silica	25.4	0.5	73	0.17

Accordingly, the deformations of the substrate will follow a modified version of the Stoney's Equation (adapted from [25]),

$$\begin{pmatrix} N_{xx} \\ N_{yy} \\ N_{xy} \end{pmatrix} = \frac{Eh_s^2}{6(1-\nu^2)}\left(\frac{h_s/2}{z_f}\right)\begin{pmatrix} 1 & \nu & 0 \\ \nu & 1 & 0 \\ 0 & 0 & 1-\nu \end{pmatrix}\begin{pmatrix} \kappa_{xx} \\ \kappa_{yy} \\ \kappa_{xy} \end{pmatrix}, \quad (1.1)$$

where N_{ij} is the ij^{th} component $(i, j = x, y)$ of stress integrated through the thickness of the film (here assumed to be small compared to the thickness of the substrate), E is the substrate's elastic modulus, ν is the substrate's Poisson ratio, h_s is the substrate thickness, z_f is the modification pattern's distance from the substrate's midplane $(h_s/2 - 100\ \mu m)$, and κ_{ij} is the ij^{th} component of average curvature. It is often more convenient and instructive to express eq (1.1) in terms of equibiaxial, antibiaxial, and shear stress components,

$$\begin{pmatrix} N_e \\ N_a \\ N_s \end{pmatrix} = \frac{Eh_s^2}{12(1-\nu^2)}\left(\frac{h_s/2}{z_f}\right)\begin{pmatrix} 1+\nu & 0 & 0 \\ 0 & 1-\nu & 0 \\ 0 & 0 & 1-\nu \end{pmatrix}\begin{pmatrix} \kappa_{xx}+\kappa_{yy} \\ \kappa_{xx}-\kappa_{yy} \\ 2\kappa_{xy} \end{pmatrix}, \quad (1.2)$$

where N_e is the equibiaxial stress component, N_a is the antibiaxial stress component, and N_s is the shear stress component. Equibiaxial stress can be understood as being responsible for creating an average curvature across the entire substrate, while anti-biaxial stress is responsible for equal but opposite curvatures introduced in orthogonal directions, and the shear stress is the responsible for producing twist about the midplane. In order to perform full figure correction using stress, in general, it is necessary to produce a rotatable stressor that contains non-equibiaxial components of stress [26].

By taking surface height measurements both before and after modification, we can relate our integrated stress terms (N_e, N_a, N_s) to the induced power and astigmatism terms (normalized Noll Zernike terms Z4, Z5, and Z6) measured by the interferometer as follows:

$$\begin{pmatrix} N_e \\ N_a \\ N_s \end{pmatrix} = \frac{Eh_s^2}{12(1-\nu^2)}\left(\frac{h_s/2}{z_f}\right)\begin{pmatrix} 1+\nu & 0 & 0 \\ 0 & 1-\nu & 0 \\ 0 & 0 & 1-\nu \end{pmatrix}\begin{pmatrix} 8\sqrt{3}A_4 \\ 4\sqrt{6}A_6 \\ 4\sqrt{6}A_5 \end{pmatrix}, \quad (1.3)$$

where A_4, A_5, and A_6 are the respective coefficients of the Z4 (power, Z_2^0), Z5 (45° astigmatism, Z_2^{-2}), and Z6 (0° astigmatism, Z_2^2) terms introduced by the applied stress field. Figure 3 depicts the surface height changes that are expected from the development of equibiaxial, antibiaxial, and shear integrated stresses. By performing this analysis for each set of modifications made, we will be able to determine overall trends and response characteristics present for each material investigated.

Downloaded From: https://www.spiedigitallibrary.org/conference-proceedings-of-spie on 24 Jan 2024
Terms of Use: https://www.spiedigitallibrary.org/terms-of-use

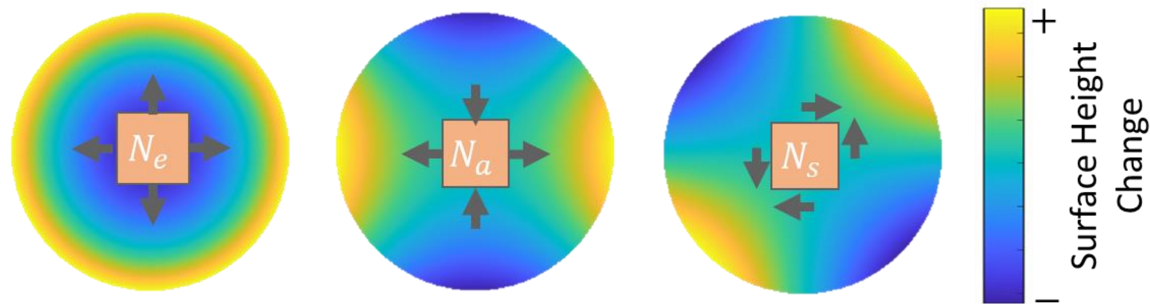

Figure 3. Surface height changes introduced by producing positive equibiaxial, antibiaxial, and shear integrated stresses. Equibiaxial integrated stress will be associated with introducing power into the surface of the substrate, while antibiaxial and shear integrated stresses will be associated introducing astigmatism into the surface.

3. RESULTS AND DISCUSSION

3.1 Effects of Repetition Rate

Figure 4 shows the results obtained for fused silica (A), ULE (B), and sapphire (C) when exposed to laser-write patterns consisting of varying repetition rates (225 kHz, 450 kHz, and 900 kHz) with a fixed spot-to-spot spacing of 50 nm. Both ULE and fused silica exhibit a similar trend in stress associated with the repetition rate. For the fastest repetition rate of 900 kHz, both materials exhibit the lowest magnitude of equibiaxial and antibiaxial stress compared to the other repetition rates. However, when exposed to ultrafast laser pulses with a repetition rate of 450 kHz and 50 nm spacing, fused silica displays a noteworthy stress versus pulse energy response that ULE does not exhibit. Initially the magnitudes of both equibiaxial and antibiaxial stress increases with increasing pulse energies. At approximately 700 nJ, the magnitude of stress begins to decrease with additional increases in pulse energies. This indicates that there are likely two competing stress generating mechanisms involved with fused silica.

At lower pulse energies and lower repetition rates, it is suspected that nanogratings begin forming and accumulating within the overlapping laser exposed regions. With increasing accumulated thermal energy, previously generated nanogratings are destroyed and a local volume of melted material begins to form surrounding the focal spot of the laser. Figure 5 shows 1 μJ modifications in fused silica with a constant spot-to-spot spacing of 50 nm and varying repetition rates through a microscope with a set of crossed polarizers; the morphology and birefringence of the modifications can be seen to vary with repetition rate. With the lowest repetition rate, we can see a high degree of birefringence within the modification zone. This is indicative of nanogratings forming within the exposed region [27]. As the repetition rate increases, the birefringence decreases which leads to less light passing through the crossed polarizers. At the highest repetition rate, irregular bubble shaped structures begin appearing within the modified zones. These structures are likely voids forming within the bulk of the material from melted material undergoing bubble nucleation and coalescence [28].

Interestingly, it is also possible to flip the sign of the equibiaxial stress generated in fused silica by pairing a high repetition rate with high pulse energies. This indicates that one of the two competing physical mechanisms for the production of equibiaxial stress likely outcompetes the other.

The measured stress for sapphire differs markedly from the results obtained for fused silica and ULE. Sapphire demonstrates a minor dependance on the repetition rate, with 900 kHz producing the least amount of stress and 450 kHz and 225 kHz producing very similar magnitudes of stress. The magnitude of stress generated for sapphire increases monotonically with increasing pulse energy until the pulse energy reaches 2.5 μJ, then exhibits a sharp decrease in the magnitude of both equibiaxial and antibiaxial stress components. It should also be noted that the magnitude of stress generated within sapphire is extremely large – on the order of kN/m versus the order of N/m for fused silica and ULE.

Downloaded From: https://www.spiedigitallibrary.org/conference-proceedings-of-spie on 24 Jan 2024
Terms of Use: https://www.spiedigitallibrary.org/terms-of-use

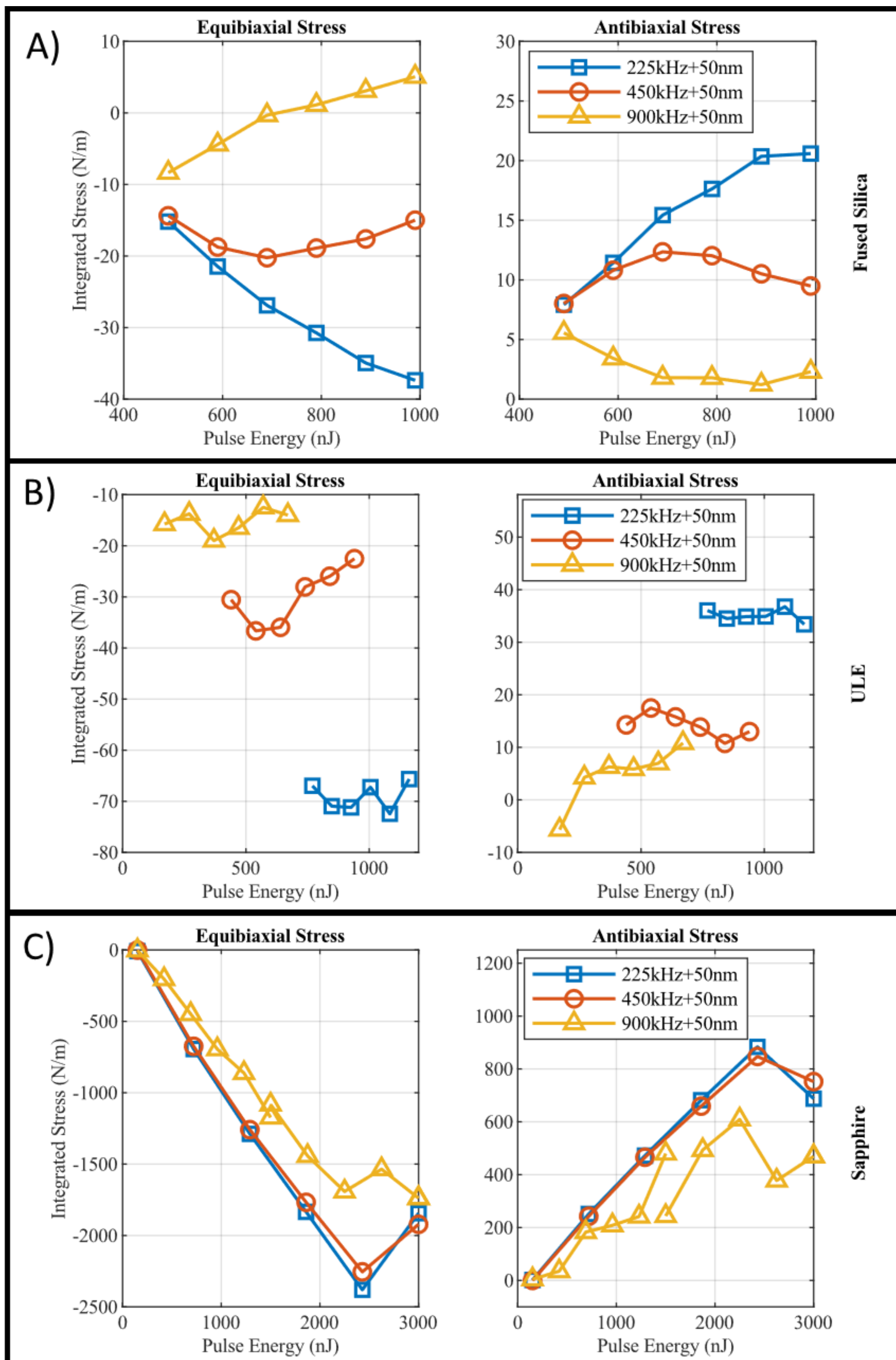

Figure 4. Equibiaxial and antibiaxial integrated stress responses for a fixed spot-to-spot spacing of 50 nm variable repetition rates for A) fused silica, B) ULE, and C) sapphire.

Downloaded From: https://www.spiedigitallibrary.org/conference-proceedings-of-spie on 24 Jan 2024
Terms of Use: https://www.spiedigitallibrary.org/terms-of-use

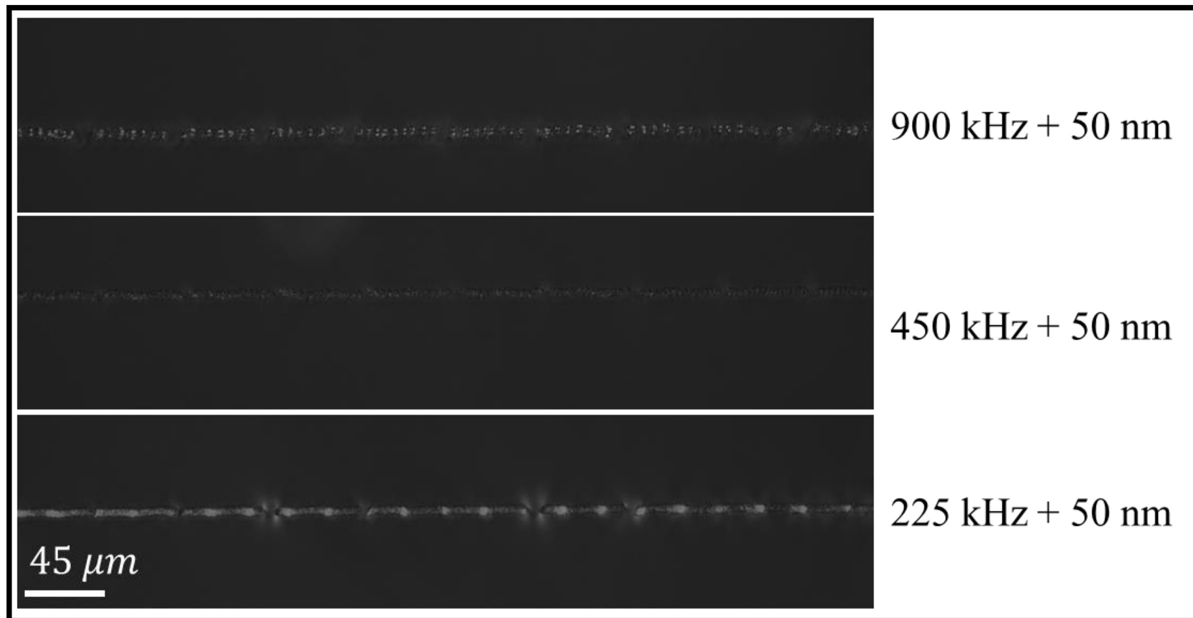

Figure 5. Crossed polarizer microscope images of the modifications in fused silica resulting from 1 μJ pulses with fixed spot-to-spot spacings of 50 nm, using various repetition rates.

3.2 Effects of Spot-to-Spot Spacing

Figure 6 shows the results obtained for fused silica (A), ULE (B), and sapphire (C) when exposed to laser-write patterns consisting of varying spot-to-spot spacings of 50 nm, 100 nm, and 200 nm with a fixed repetition rate of 225 kHz. For fused silica, as the spot-to-spot spacing decreases from 200 nm to 50 nm, the magnitude of equibiaxial and antibiaxial stress generated increases. At higher pulse energies, by initially doubling the number of laser spots (i.e. going from 200 nm to 100 nm spot-to-spot spacing) we increase the magnitude of equibiaxial and antibiaxial stress generated by $1.83\times$ and $2.36\times$ respectively. This effect appears to saturate rather quickly, as an additional doubling of laser modifications leads to a modest increase of $1.09\times$ and $1.07\times$.

ULE exhibits the opposite trend as fused silica. As the spot-to-spot spacing decreases from 200nm to 50nm, the magnitude of stress generated decreases. Additional laser pulses appear to destroy whatever material modification is responsible for the stress generation in ULE for these particular laser processing parameters. Despite having very similar material properties to fused silica, ULE's response to ultrafast laser stressing is noticeably different.

Sapphire shows a similar trend to fused silica, albeit not as drastic. At higher pulse energies, with decreasing spot-to-spot spacing, the magnitude of stress generated increases rather monotonically – with the initial doubling of spots producing a $1.35\times$ and $1.46\times$ increase in the magnitude of equibiaxial and antibiaxial stress respectively. A subsequent doubling of laser spots leads to an increase of $1.31\times$ and $1.41\times$. This indicates that we may have underdeveloped material modifications, and we may be able to increase the magnitude of stress generated even further with additional overlapping laser pulses.

Downloaded From: https://www.spiedigitallibrary.org/conference-proceedings-of-spie on 24 Jan 2024
Terms of Use: https://www.spiedigitallibrary.org/terms-of-use

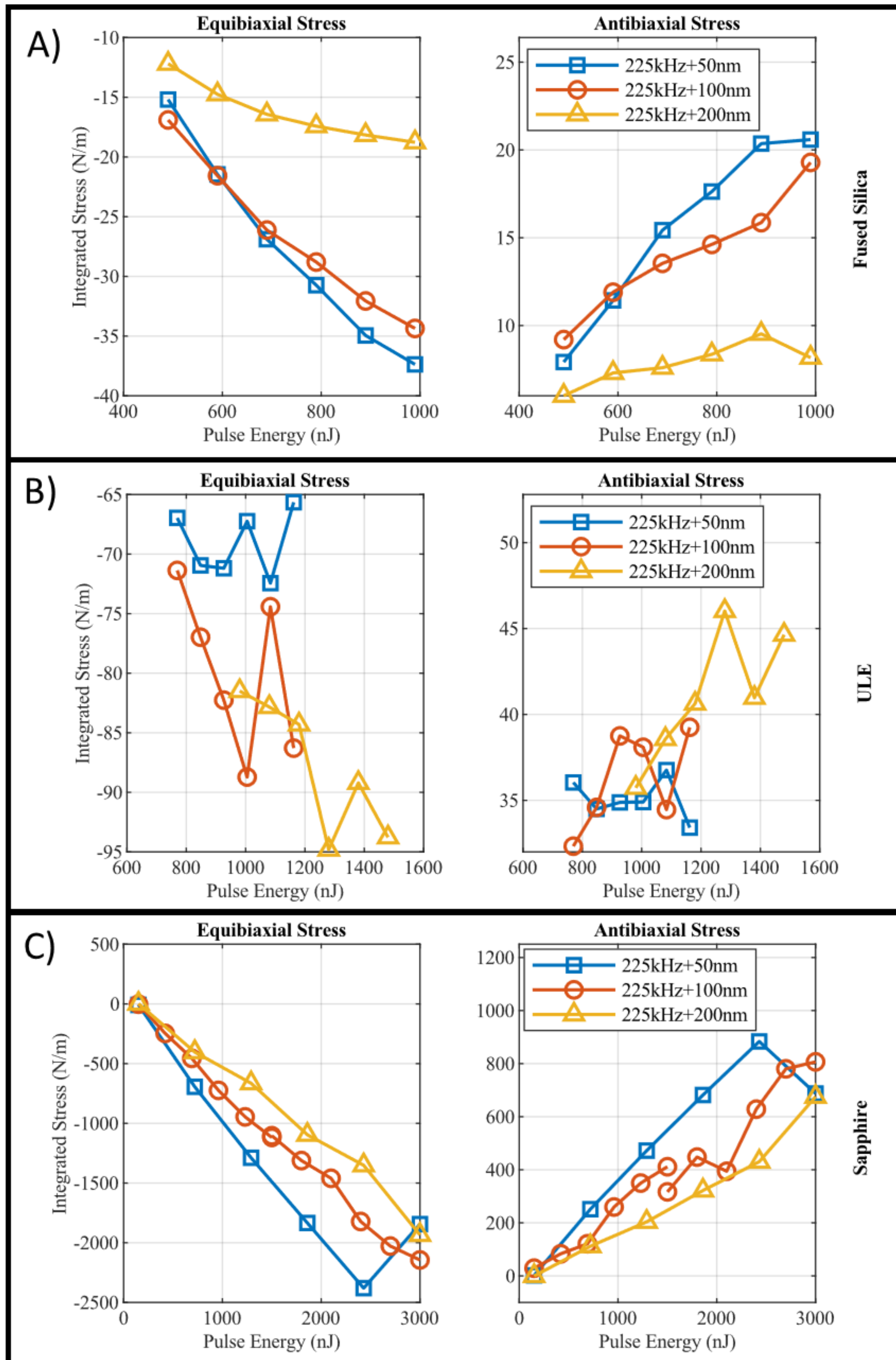

Figure 6. Equibiaxial and antibiaxial integrated stress responses for a fixed repetition rate of 225 kHz and variable spot-to-spot spacings for A) fused silica, B) ULE, and C) sapphire.

Downloaded From: https://www.spiedigitallibrary.org/conference-proceedings-of-spie on 24 Jan 2024
Terms of Use: https://www.spiedigitallibrary.org/terms-of-use

3.3 Integrated Stress Response of Eagle XG

Figure 7 shows the initial results obtained for Eagle XG when exposed to several laser write conditions. Due to time and equipment constraints, only some of the repetition rate and spot-to-spot spacing pairs were able to be investigated for Eagle XG. These samples were exposed to three different pairs of repetition rates and spot-to-spot spacings: $(225\text{ kHz} + 100\text{ nm})$, $(450\text{ kHz} + 100\text{ nm})$, and $(900\text{ kHz} + 50\text{ nm})$. Interestingly, all combinations tested led to the generation of positive equibiaxial stress, which is in stark contrast to the other materials tested – with the only exception being for fused silica at 900 kHz with 50 nm spacing and higher pulse energies. Despite having the same number of pulses, the 450 kHz results produced significantly more equibiaxial stress and the opposite sign of antibiaxial stress when compared to the 225 kHz results. Excluding the 225 kHz results, both remaining combinations show an increasing magnitude of equibiaxial and antibiaxial stress generated as the pulse energy is increased.

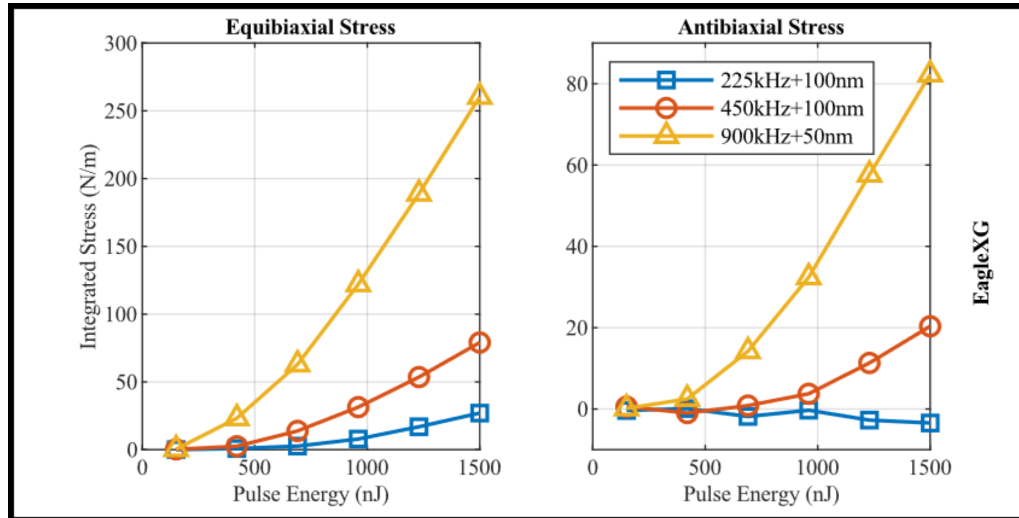

Figure 7. Eagle XG equibiaxial and antibiaxial stress responses for various laser processing parameters.

3.4 Theoretical Flattening of Commercial Sapphire and Eagle XG Wafers

Using the maximal stress states achieved from the data presented in sections 3.1, 3.2, and 3.3, a theoretical set of calibration constants used in ULSF (see ref [24] for more details) was produced for sapphire and Eagle XG. This corresponds to process parameters of 225 kHz, 50 nm spot-to-spot spacing, and 2430 nJ for sapphire, and 900 kHz, 50 nm spot-to-spot spacing, and 1500 nJ for Eagle XG. An Eagle XG (100 mm diameter, 0.4 mm thick) and a sapphire (c-plane, DSP, 100 mm diameter, 0.6 mm thick) wafer were each measured on the interferometer; the generated calibration constants were used to produce a laser correction pattern that is expected to flatten the unwanted surface height errors present on the wafers. The measured surface height profiles of both wafers are shown in Figure 8. The expected eMRRs for the ULSF process applied to both wafers is shown in Table 2. The values displayed in Table 2 are an upper limit to what is possible for these two wafers, since the ULSF process has historically required at least a first and second pass to achieve the desired flatness. It should also be noted that the eMRR is dependent on the desired surface change, with higher order Zernike terms requiring more complicated stress patterns to correct for.

For the first pass, it is anticipated that sapphire will achieve an eMRR greater than $30\text{ mm}^3/\text{hr}$, which is extremely fast when compared to other methods of deterministically figuring sapphire, such as magnetorheological fluid polishing (MRR of ~$0.19\text{ mm}^3/\text{hr}$ for 100 mm diameter substrate) [29]. The eMRR of Eagle XG is expected to be greater than $200\text{ mm}^3/\text{hr}$. Eagle XG showcases a higher theoretical eMRR than sapphire in this example due to the starting shape of the wafer and the fact that the substrate is more compliant to applied stresses since it is thinner and less stiff. The Eagle XG wafer is dominated primarily by pure astigmatism, which requires minimal laser writing to correct for. The initial surface profile of the sapphire wafer is more complicated, and requires additional laser write paths to appropriately compensate.

Downloaded From: https://www.spiedigitallibrary.org/conference-proceedings-of-spie on 24 Jan 2024
Terms of Use: https://www.spiedigitallibrary.org/terms-of-use

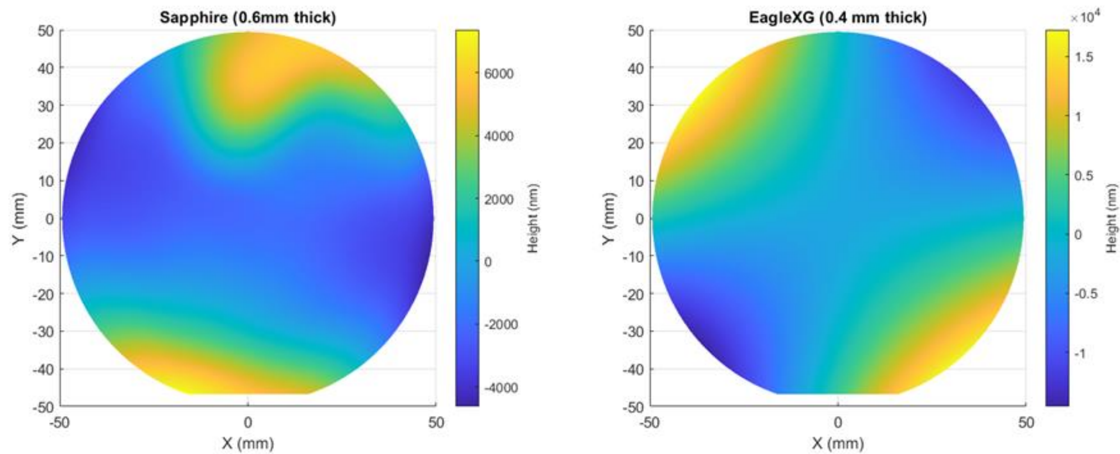

Figure 8: Initial surface height profiles of the sapphire and Eagle XG wafers.

Table 2. Estimated ULSF process performance.

Material	Estimated eMRR (mm^3/hr)	Estimated Process Time (min)
Sapphire	34.6	95
Corning Eagle XG	228.8	34

4. CONCLUSIONS AND FUTURE WORK

With the ability to produce stress within all materials tested, ULSF has a path forward to produce desired substrate curvature changes in fused silica, Corning Eagle XG, Corning ULE, and sapphire. It was found that the magnitude of stress generated by ultrafast laser pulses focused into dielectric materials depends on the laser repetition rate, the spot-to-spot spacing, and pulse energy. The choice of dielectric material also highly impacts the magnitude of stresses generated. Theoretical ULSF recipes were created for commercial sapphire and Eagle XG wafers using the highest magnitude stress achieved during the investigation for each material respectively. eMRRs of greater than $30\ mm^3/hr$ are expected to be attainable through ULSF for sapphire, which is far larger than most deterministic figuring methods. Additionally, eMRRs greater than $200\ mm^3/hr$ are expected for Eagle XG.

For constant pulse-to-pulse spacing, fused silica exhibited a notable transition at high pulse energies from negative equibiaxial stress to positive equibiaxial stress as the repetition rate increased. We speculate that this transition indicates that the mechanism involved in the stress generation can likely be decomposed into two competing physical changes. The first consists of a structural change (i.e. densification and nanograting formation) that occurs when the material is exposed to low laser powers. As the repetition rate increases, the material surrounding the focal volume begins to accumulate thermal energy which leads to a melt zone forming. This melted region likely destroys some of the previously formed structural modifications, lowering the magnitude of stress, while additionally producing its own stress through a quenching of the melted zone. This theory is supported by the fact that we initially achieve birefringent zones within the modifications at low repetition rates, which subsequently disappear as the repetition rate is increased. Additionally at the highest repetition rate, the structure of the modifications appears to have taken on the form of many distributed bubbles indicating that a melt region has formed. The exact mechanism responsible for the stress generation may impact additional downstream qualities, such as coefficient of thermal expansion or bending strength, and should be further investigated.

Future work will involve demonstrating actual ULSF corrections of commercially available wafers for each material presented in this investigation. Additionally, the stability of the laser modifications and the impact that these modifications have on the bending strength of the materials tested will be explored. The results of these future investigations may influence the choice of laser modifications that are desirable for different end-use cases of the ULSF process.

Downloaded From: https://www.spiedigitallibrary.org/conference-proceedings-of-spie on 24 Jan 2024
Terms of Use: https://www.spiedigitallibrary.org/terms-of-use

5. ACKNOWLEDGEMENTS

The authors would like to thank Ian Arnold for valuable equipment assistance and sample preparation. The authors would also like to thank Caroline Humphreys, Carolyn Hokin, Josh Richards for assistance with experimental data collection.

DISTRIBUTION STATEMENT A. Approved for public release. Distribution is unlimited.

This material is based upon work supported by the Under Secretary of Defense for Research and Engineering under Air Force Contract No. FA8702-15-D-0001. Any opinions, findings, conclusions or recommendations expressed in this material are those of the author(s) and do not necessarily reflect the views of the Under Secretary of Defense for Research and Engineering.

© 2023 Massachusetts Institute of Technology.

Delivered to the U.S. Government with Unlimited Rights, as defined in DFARS Part 252.227-7013 or 7014 (Feb 2014). Notwithstanding any copyright notice, U.S. Government rights in this work are defined by DFARS 252.227-7013 or DFARS 252.227-7014 as detailed above. Use of this work other than as specifically authorized by the U.S. Government may violate any copyrights that exist in this work.

REFERENCES

1. Y. Bellouard, E. Barthel, A. A. Said, M. Dugan, and P. Bado, "Scanning thermal microscopy and Raman analysis of bulk fused silica exposed to lowenergy femtosecond laser pulses," Opt. Express **16**, 19520 (2008).
2. Y. Bellouard, T. Colomb, C. Depeursinge, M. Dugan, A. A. Said, and P. Bado, "Nanoindentation and birefringence measurements on fused silica specimen exposed to low-energy femtosecond pulses," Opt. Express **14**, 8360 (2006).
3. A. Champion and Y. Bellouard, "Direct volume variation measurements in fused silica specimens exposed to femtosecond laser," Opt. Mater. Express **2**, 789–798 (2012).
4. E. Fertein, C. Przygodzki, H. Delbarre, A. Hidayat, M. Douay, and P. Niay, "Refractive-index changes of standard telecommunication fiber through exposure to femtosecond laser pulses at 810 cm," Appl. Opt. **40**, 3506 (2001).
5. M. Kamata and M. Obara, "Control of the refractive index change in fused silica glasses induced by a loosely focused femtosecond laser," Appl. Phys. A **78**, 85–88 (2004).
6. M. Sakakura and M. Terazima, "Initial temporal and spatial changes of the refractive index induced by focused femtosecond pulsed laser irradiation inside a glass," Phys. Rev. B **71**, 024113 (2005).
7. Y. Liao, W. Pan, Y. Cui, L. Qiao, Y. Bellouard, K. Sugioka, and Y. Cheng, "Formation of in-volume nanogratings with sub-100-nm periods in glass by femtosecond laser irradiation," Opt. Lett. **40**, 3623 (2015).
8. C. Hnatovsky, R. S. Taylor, P. P. Rajeev, E. Simova, V. R. Bhardwaj, D. M. Rayner, and P. B. Corkum, "Pulse duration dependence of femtosecond-laser-fabricated nanogratings in fused silica," Appl. Phys. Lett. **87**, 014104 (2005).
9. Y. Shimotsuma, P. G. Kazansky, J. Qiu, and K. Hirao, "Self-Organized Nanogratings in Glass Irradiated by Ultrashort Light Pulses," Phys. Rev. Lett. **91**, 247405 (2003).
10. Y. Shimotsuma, M. Sakakura, P. G. Kazansky, M. Beresna, J. Qiu, K. Miura, and K. Hirao, "Ultrafast Manipulation of Self-Assembled Form Birefringence in Glass," Adv. Mater. **22**, 4039–4043 (2010).
11. K. Cvecek, I. Miyamoto, and M. Schmidt, "Gas bubble formation in fused silica generated by ultra-short laser pulses," Opt. Express **22**, 15877 (2014).
12. E. O. Kissi and Y. Bellouard, "Self-organized nanostructures forming under high-repetition rate femtosecond laser bulk-heating of fused silica," Opt. Express **26**, 14024 (2018).
13. S. Richter, S. Döring, F. Burmeister, F. Zimmermann, A. Tünnermann, and S. Nolte, "Formation of periodic disruptions induced by heat accumulation of femtosecond laser pulses," Opt. Express **21**, 15452 (2013).
14. Y. Dai, A. Patel, J. Song, M. Beresna, and P. G. Kazansky, "Void-nanograting transition by ultrashort laser pulse irradiation in silica glass," Opt. Express **24**, 19344 (2016).
15. C. Hnatovsky, R. S. Taylor, E. Simova, V. R. Bhardwaj, D. M. Rayner, and P. B. Corkum, "Polarization-selective etching in femtosecond laser-assisted microfluidic channel fabrication in fused silica," Opt. Lett. **30**, 1867 (2005).
16. D. Wortmann, J. Gottmann, N. Brandt, and H. Horn-Solle, "Micro- and nanostructures inside sapphire by fs-laser irradiation and selective etching," Optics Express **16**, (2008).
17. M. Beresna, M. Gecevičius, and P. G. Kazansky, "Polarization sensitive elements fabricated by femtosecond laser nanostructuring of glass [Invited]," Opt. Mater. Express **1**, 783 (2011).
18. J. Zhang, M. Gecevičius, M. Beresna, and P. G. Kazansky, "5D Data Storage by Ultrafast Laser Nanostructuring in Glass," in CLEO (OSA, 2013), p. CTh5D.9.

Downloaded From: https://www.spiedigitallibrary.org/conference-proceedings-of-spie on 24 Jan 2024
Terms of Use: https://www.spiedigitallibrary.org/terms-of-use

19. H. Huang, L.-M. Yang, and J. Liu, "Direct welding of fused silica with femtosecond fiber laser," in Proc. SPIE (2012), p. 824403.
20. R. M. Carter, J. Chen, J. D. Shephard, R. R. Thomson, and D. P. Hand, "Picosecond laser welding of similar and dissimilar materials," Appl. Opt. **53**, 4233 (2014).
21. G. Zhang and G. Cheng, "Direct welding of glass and metal by 1 kHz femtosecond laser pulses," Appl. Opt. **54**, 8957 (2015).
22. Y. Bellouard, A. Champion, B. McMillen, S. Mukherjee, R. R. Thomson, C. Pépin, P. Gillet, and Y. Cheng, "Stress-state manipulation in fused silica via femtosecond laser irradiation," Optica **3**, 1285 (2016).
23. B. D. Chalifoux, I. J. Arnold, and K. A. Laverty, "Ultrafast laser strain generation for nanometer-precision alignment of optical components," in Proc. SPIE (2021).
24. B. D. Chalifoux, K. A. Laverty, and I. J. Arnold, "Ultrafast laser stress figuring for accurate deformation of thin mirrors," Opt. Express **30**, 17780 (2022).
25. L. B. Freund and S. Suresh, Thin Film Materials: Stress, Defect Formation and Surface Evolution, 1st ed. (Cambridge University Press, 2004).
26. Y. Yao, B. Chalifoux, R. K. Heilmann, and M. L. Schattenburg, "Stress tensor mesostructures for deterministic figuring of thin substrates," Optica **9**, 438 (2022).
27. L. P. R. Ramirez, M. Heinrich, S. Richter, F. Dreisow, R. Keil, A. V. Korovin, U. Peschel, S. Nolte, and A. Tünnermann, "Tuning the structural properties of femtosecond-laser-induced nanogratings," Appl. Phys. A **100**, 1–6 (2010).
28. Y. Bellouard and M.-O. Hongler, "Femtosecond-laser generation of self-organized bubble patterns in fused silica," Opt. Express **19**, 6807 (2011).
29. Y. Tian, S. Qiao, S. Guo, Y. Hou, and F. Shi, "Combined polishing process of a sapphire aspherical component based on temperature-controlled magnetorheological processing," Appl. Opt. **62**, 805 (2023).

Downloaded From: https://www.spiedigitallibrary.org/conference-proceedings-of-spie on 24 Jan 2024
Terms of Use: https://www.spiedigitallibrary.org/terms-of-use